# Customizing the Angular Memory Effect for Scattering Media

Hasan Yılmaz,[1,2] Matthias Kühmayer,[3] Chia Wei Hsu,[4] Stefan Rotter,[3] and Hui Cao[1,*]

[1]*Department of Applied Physics, Yale University, New Haven, Connecticut 06520, USA*
[2]*Institute of Materials Science and Nanotechnology, National Nanotechnology Research Center (UNAM), Bilkent University, 06800 Ankara, Turkey*
[3]*Institute for Theoretical Physics, Vienna University of Technology (TU Wien), A-1040 Vienna, Austria*
[4]*Ming Hsieh Department of Electrical and Computer Engineering, University of Southern California, Los Angeles, California 90089, USA*

(Received 5 November 2020; accepted 11 May 2021; published 15 July 2021)

The memory effect in disordered systems is a key physical phenomenon that has been employed for optical imaging, metrology, and communication through opaque media. Under the conventional memory effect, when the incident beam is tilted slightly, the transmitted pattern tilts in the same direction. However, the "memory" is limited in its angular range and tilt direction. Here, we present a general approach to customize the memory effect by introducing an angular memory operator. Its eigenstates possess perfect correlation for tilt angles and directions that can be arbitrarily chosen separately for the incident and transmitted waves, and can be readily realized with wave front shaping. This work reveals the power of wave front shaping in creating any desired memory for applications of classical and quantum waves in complex systems.

DOI: 10.1103/PhysRevX.11.031010 Subject Areas: Optics, Photonics

## I. INTRODUCTION

Multiple scattering of light in disordered media such as white paint, paper, and biological tissue randomizes the propagation of waves and scrambles the spatial information carried by an incident beam. Once the thickness of a sample exceeds the transport mean free path, the information about the incident direction is lost, and light waves are scattered in all directions. While the interference of these scattered waves forms a random grainy pattern (speckle) in transmission, some memory is retained, as a result of the deterministic scattering process [1–3]. One prominent example is the angular memory effect: if the incident wave front of a coherent beam is tilted by a small angle, the transmitted wave front is tilted by the same amount in the same direction. Both classical and quantum waves possess such a memory [4–8], which persists even in the deep diffusive regime where forward-scattered waves are negligible and the information of the original propagation direction is lost already [9–12]. In this way the angular memory effect provides unique access to the transmitted far-field pattern behind a disordered sample, which can be conveniently scanned by tilting the incident wave front. This feature has enabled a wide range of applications in imaging, sensing, and optical metrology through turbid media [13–31].

While the angular memory effect exists for any incident wave front, it is severely limited by the small angular range of $\lambda/(2\pi L)$ for a diffusive sample of thickness $L$ at wavelength $\lambda$. Various schemes have been developed recently to increase the range of the angular memory effect, e.g., by time gating [32], spatial filtering [33] of the transmitted light or disorder engineering [34], as well as by combining it with the translational memory effect [6,35,36] through a forward-scattering medium, or by coupling light into high-transmission eigenchannels in a diffusive medium [37]. What all these works have in common, however, is that they are constrained by the restrictions of the conventional memory effect for which the output wave front tilts by the same angle and in the same direction as the input wave front. To overcome these inherent limitations, we consider here a radical expansion of the angular memory effect by addressing the following questions. Is it possible to achieve a tilt in the output wave front along a different direction and/or with a different angle as compared to that of the input wave front? Can "perfect correlation" be obtained at arbitrarily chosen tilt angles which will effectively increase the memory effect range well beyond the conventional one?

The affirmative answers we provide here to these questions involve a customization of the angular memory by shaping the incident wave front of a coherent beam. For this purpose, we introduce an angular memory operator whose eigenvectors provide perfect memory for arbitrarily

*hui.cao@yale.edu

chosen input and output tilt angles of the incoming and outgoing wave fronts. By launching coherent light through such an eigenvector into a diffusive system, we experimentally demonstrate that the transmitted wave front can even tilt in the opposite direction to that of the incident wave front. Moreover, we show that such correlations can be achieved simultaneously at different input and output angles and that the corresponding tilt angles at both the input and output may well exceed the conventional angular memory range. Our methodology is applicable to other types of memory effects and in different kinds of complex systems such as chaotic cavities or multimode fibers. It provides a general framework for designing and creating desired memories for various applications in imaging, metrology, and communication through complex media.

## II. ANGULAR MEMORY OPERATOR

To customize the angular memory effect, we first define a correlation coefficient that quantifies the similarity between a transmitted field pattern $t|\psi\rangle$ and one with arbitrary tilt angles $\theta_i$, $\theta_o$ of the input and output wave fronts, $X^\dagger(\theta_o)tX(\theta_i)|\psi\rangle$:

$$C_E(\theta_i,\theta_o) \equiv \frac{\langle\psi|t^\dagger X^\dagger(\theta_o)tX(\theta_i)|\psi\rangle}{\sqrt{\langle\psi|t^\dagger t|\psi\rangle\langle\psi|X^\dagger(\theta_i)t^\dagger tX(\theta_i)|\psi\rangle}}, \quad (1)$$

where $\psi$ denotes the input field, $t$ the field transmission matrix of the scattering medium, and $X(\theta_i)$ and $X^\dagger(\theta_o)$ are rotation operators that tilt the incoming and outgoing field profiles by angles $\theta_i$ and $\theta_o$, respectively. See Sec. D of the Supplemental Material for a detailed description of the rotation operator and how to avoid edge effects [38].

For the conventional angular memory effect the input and the output angles are equal, $\theta_i = \theta_o$, and within the angular range of $\lambda/(2\pi L)$ for a diffusive slab of thickness $L$, as sketched in Fig. 1(a). To achieve memory for arbitrary $\theta_i$ and $\theta_o$, we tailor the incident wave front $\psi$ to maximize $|C_E(\theta_i,\theta_o)|$ without compromising the overall transmittance. While nonlinear optimization methods can be employed to search for an optimal $\psi$, they are unlikely to find the global maximum in such a high-dimensional search. We thus introduce here an angular memory operator whose eigenvectors maximize the correlations for any chosen input and output tilt angles. Figure 1(b) shows, as an example, that while the input wave front is tilted in the horizontal ($x$) direction, the output wave front tilts in the vertical ($y$) direction, and input and output wave fronts tilt by different angles.

To build such an angular memory operator, we start with the expression $Q_0 \equiv t^\dagger X^\dagger(\tilde{\theta}_o)tX(\tilde{\theta}_i)$ [appearing in the numerator of Eq. (1)], with its eigenvectors given by $Q_0|V_n^{(0)}\rangle = \alpha_n^{(0)}|V_n^{(0)}\rangle$. In our angular memory operator, $\tilde{\theta}_o$ and $\tilde{\theta}_i$ represent the output and input angles we choose for customizing the angular memory effect, respectively. Using these eigenvectors $|V_n^{(0)}\rangle$ as input wave fronts, the numerator of the correlation coefficient $C_E$ in Eq. (1) equals to the corresponding complex-valued eigenvalues $\alpha_n^{(0)}$. Correspondingly, the eigenvectors of $Q_0$ with large $|\alpha_n^{(0)}|$ have a large numerator of $|C_E|$. As it turns out, this does not necessarily enhance $|C_E|$, because the eigenvectors may achieve a large numerator of $|C_E|$ already by coupling light into high-transmission eigenchannels. A higher transmission increases, however, not only the numerator but also the denominator of $|C_E|$ without necessarily increasing the similarity between $t|V_n^{(0)}\rangle$ and $X^\dagger(\tilde{\theta}_o)tX(\tilde{\theta}_i)|V_n^{(0)}\rangle$.

To enhance $|C_E|$ instead of just its numerator, we adapt the angular memory operator in the following way:

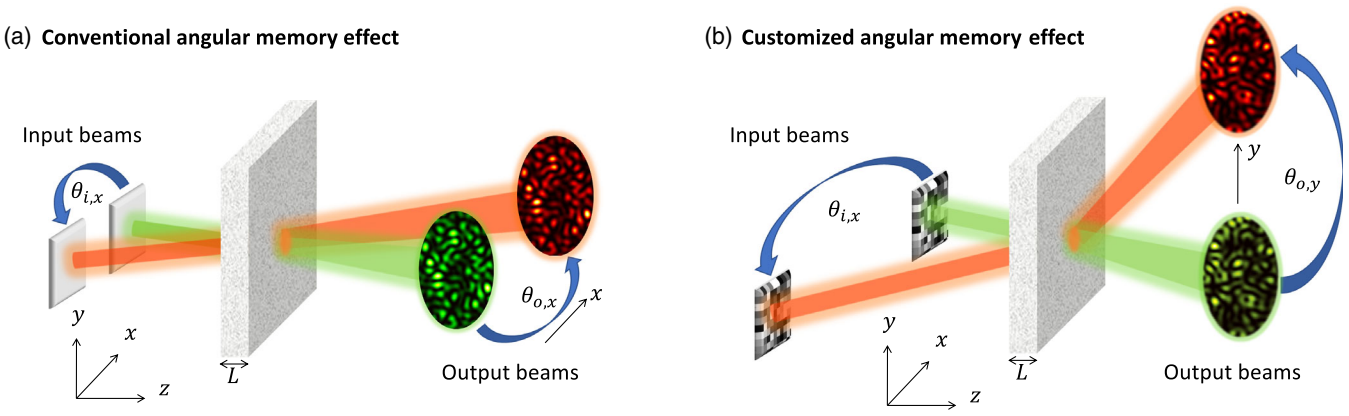


FIG. 1. Conventional versus customized angular memory effect. (a) Schematic of the conventional angular memory effect: a beam of coherent light (wavelength $\lambda$) is impinging onto a diffusive slab of thickness $L$. When the incident beam is tilted by a small angle $\theta_{i,x} < \lambda/(2\pi L)$, the transmitted pattern tilts in the same direction by $\theta_{o,x} = \theta_{i,x}$. (b) Schematic of the customized angular memory effect: both the input and the output tilt angles can be chosen arbitrarily for a special incident wave front. In this example, when the input wave front is tilted by $\theta_{i,x}$ in $\hat{x}$ direction, the output wave front tilts in $\hat{y}$ direction by $|\theta_{o,y}| \neq |\theta_{i,x}|$.

$$Q(\tilde{\theta}_i, \tilde{\theta}_o) \equiv (t^\dagger t)^{-1} t^\dagger X^\dagger(\tilde{\theta}_o) t X(\tilde{\theta}_i). \quad (2)$$

The additional term $(t^\dagger t)^{-1}$ counterbalances the increase of the numerator that would result from an increase in the transmittance only. Alternatively, one can also counterbalance the transmittance by using the term $\{[X^\dagger(\tilde{\theta}_o) t X(\tilde{\theta}_i)]^\dagger X^\dagger(\tilde{\theta}_o) t X(\tilde{\theta}_i)\}^{-1}$, which results in a similar expression in Eq. (2) (see Sec. E in the Supplemental Material for the derivation [38]). Here, we restrict ourselves to the case where the number of output channels $N_o$ in the transmission matrix $t$ is no less than the number of input channels $N_i$, i.e., $N_o \geq N_i$. This situation is typically realized in experimental measurements of a transmission matrix $t$, where the number of controlled input channels $N_i$ (i.e., number of columns of $t$) does not exceed the number of detected output channels $N_o$ (i.e., number of rows of $t$), and guarantees that the expression $(t^\dagger t)^{-1} t^\dagger$ in Eq. (2) (left inverse of $t$) exists. Moreover, when the number of input and output channels is the same, $N_o = N_i$, the left inverse just equals $t^{-1}$, and the angular memory operator in Eq. (2) reduces to the simple expression $Q(\tilde{\theta}_i, \tilde{\theta}_o) = t^{-1} X^\dagger(\tilde{\theta}_o) t X(\tilde{\theta}_i)$, with its eigenvectors $Q(\tilde{\theta}_i, \tilde{\theta}_o)|V_n\rangle = \alpha_n |V_n\rangle$ satisfying $X^\dagger(\tilde{\theta}_o) t X(\tilde{\theta}_i)|V_n\rangle = \alpha_n t|V_n\rangle$. More precisely, tilted output field patterns $X^\dagger(\tilde{\theta}_o) t X(\tilde{\theta}_i)|V_n\rangle$'s are identical to the original ones $t|V_n\rangle$'s, aside from a constant factor $\alpha_n$. The correlation coefficient thus reaches its maximal value, $|C_E| = 1$. Hence, with the number of input and output channels being equal, $N = N_i = N_o$, the $N$ eigenvectors of $Q$, regardless of their associated eigenvalues, provide $N$ incident wave fronts to create $N$ perfectly correlated pairs of input-output field patterns for the chosen angles $\tilde{\theta}_i$ and $\tilde{\theta}_o$. We note that eigenvectors of a different operator were recently developed to correlate the transmitted field profile of a scattering medium to that of free space [39].

When $N_o > N_i$, the eigenstates of $Q$ satisfy $t^\dagger X^\dagger(\tilde{\theta}_o) t X(\tilde{\theta}_i)|V_n\rangle = \alpha_n t^\dagger t|V_n\rangle$, which is to say that the outputs projected by $t^\dagger$ have perfect correlation. The unprojected outputs can still exhibit high correlations, even though less than unity, and the eigenstate with the highest possible correlation will be shown below.

## III. EXPERIMENTS

Next, we construct the angular memory operator $Q$ using our experimentally measured transmission matrix of a diffusive sample. Our sample is a densely packed zinc oxide (ZnO) nanoparticle layer on a cover slip. The layer thickness is about 10 $\mu$m, much larger than the transport mean free path $l_t \sim 1$ $\mu$m, such that the light transport in the ZnO layer is diffusive. The transmission matrix $t$ is measured with an interferometer setup shown in Fig. S1 of the Supplemental Material [38]. A linearly polarized monochromatic laser beam at wavelength $\lambda = 532$ nm is split and injected into the two arms of the interferometer. A spatial light modulator (SLM) in the sample arm prepares the phase front of the light field, which is then projected onto the front surface of the ZnO layer. The light transmitted through the sample combines with the reference beam from the other arm. Their interference pattern is recorded by a CCD camera placed in the far field of the sample. The phase front of the output field from the sample is recovered from four interference patterns acquired with varying global phases displayed on the SLM. The reference beam has a flat phase front, allowing the retrieval of the relative phase between output fields at different locations in the far field. This information is critical to the construction of the angular memory operator, which requires measurement of the correlation between fields at different output angles (corresponding to different far-field locations). In contrast to the common-path interferometry method [37,40,41], which measures only the relative phases between different input channels to the same output channel (i.e., only relative phases between the columns of $t$), our method measures the phase differences between both columns and rows of the transmission matrix.

We construct $Q(\tilde{\theta}_i, \tilde{\theta}_o)$ from the measured $t$. Experimentally we record a part of the total transmission matrix, with the number of input channels $N_i$ equal to the number of SLM macropixels and the number of output channels $N_o$ being determined by the detection area on the camera. Figure 2 shows an example with $N_i = 1024$ and $N_o = 4096$. Since the camera pixel size is smaller than the average speckle grain size, the number of speckle grains at the output is 455. The transverse plane $x$-$y$ in Fig. 2 is parallel to the sample surface. We choose opposite tilts for the field profiles at the input and the output of the scattering sample, $\tilde{\theta}_{i,y} = -7.8°$ and $\tilde{\theta}_{o,y} = 7.1°$. This means when the incoming wave front is tilted in the $-y$ direction by 7.8°, the outgoing wave front tilts in $+y$ by 7.1°. We find the eigenvectors of such $Q$, and set the input wave front to its first eigenvector $|V_1\rangle$ with the largest $|\alpha_1|$. Because $N_i < N_o$, $|C_E|$ does not reach unity, but it increases with $|\alpha_n|$ and has the maximum at $|\alpha_1|$ (see Fig. S3 in the Supplemental Material [38]). Then we scan the tilt angle of the input wave front $\theta_{i,y}$ along the $y$ axis and calculate the output wave front using the measured transmission matrix $t$. After tilting the output wave front by an angle $\theta_{o,y}$ in $y$, we calculate its correlation $C_E$ with the original output wave front without tilting the input.

## IV. RESULTS AND DISCUSSION

Figure 2(a) shows $|C_E|$ for each pair of $\theta_{i,y}$ and $\theta_{o,y}$ in the range of $-10°$ and 10°. The conventional angular memory effect is buried in the correlation at the origin $C_E(0,0)$, because its range is only about 1° and is less than the step size (2.5°) of $\theta_{i,y}$ and $\theta_{o,y}$. Therefore, the chosen angles $\tilde{\theta}_{i,y}$ and $\tilde{\theta}_{o,y}$ are well beyond the conventional angular memory effect range. Figure 2(b) shows the output wave front without tilting input or output, $\theta_{i,y} = 0$ and $\theta_{o,y} = 0$. When the input wave front is tilted by $\theta_{i,y} = \tilde{\theta}_{i,y} = -7.8°$ and

output by $\theta_{o,y} = \tilde{\theta}_{o,y} = 7.1°$, the output field pattern in Fig. 2(c) is very similar to the original pattern in Fig. 2(b). In contrast, the output field pattern in Fig. 2(d) is completely different for $\theta_{i,y} = 2.6° \neq \tilde{\theta}_{i,y}$ and $\theta_{o,y} = 2.4° \neq \tilde{\theta}_{o,y}$.

In this example (Fig. 2), the input and the output wave fronts tilt in opposite direction along the $y$ axis. In Fig. S4 of the Supplemental Material, we present examples where the input wave front is tilted in the $y$ direction, while the output wave front tilts in the $x$ direction or in the diagonal direction $\hat{x} + \hat{y}$ [38]. As described above, when $N_o \leq N_i$, all eigenvectors of $Q(\tilde{\theta}_i, \tilde{\theta}_o)$ should achieve perfect memory with $|C_E(\tilde{\theta}_i, \tilde{\theta}_o)| = 1$ for any input and output tilt angles $\tilde{\theta}_i$ and $\tilde{\theta}_o$. Figure 3(a) shows that such perfect correlation is indeed observed when we reduce $N_o$ to $1024 = N_i$. For any chosen pair of $\tilde{\theta}_i$ and $\tilde{\theta}_o$, the corresponding 1024 eigenstates of $Q$ all have $|C_E| = 1$, as shown in Fig. 3(c).

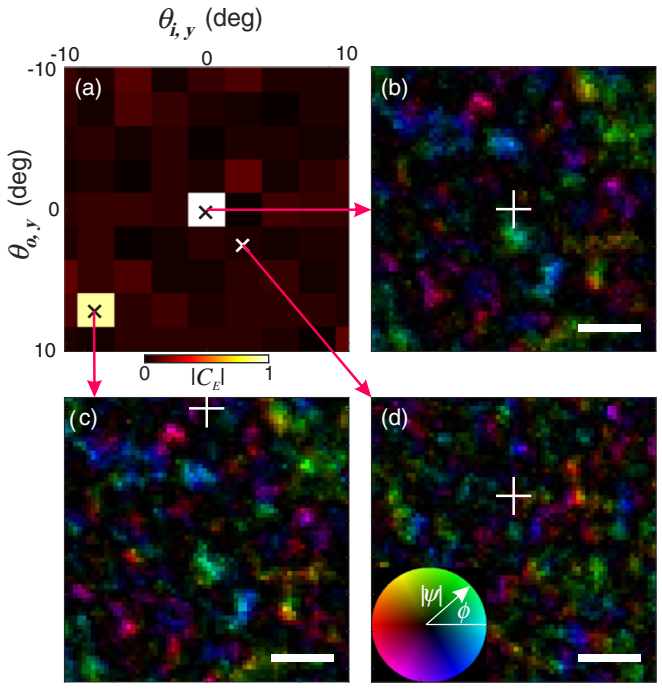


FIG. 2. Angular correlation of output field patterns. (a) Correlation coefficient $|C_E(\theta_{i,y}, \theta_{o,y})|$ for the incident wave front given by the eigenvector $|V_1\rangle$ of the angular memory operator $Q(\tilde{\theta}_{i,y} = -7.8°, \tilde{\theta}_{o,y} = 7.1°)$ with the largest eigenvalue amplitude $|\alpha_1|$. The number of controlled input channels is $N_i = 1024$, and the number of detected output channels is $N_o = 4096$. (b) With the incident wave front $|V_1\rangle$, the transmitted field pattern in the far field is represented with the field amplitude by brightness and the phase by color using the color wheel in (d). The horizontal and vertical axes denote $k_{o,x}$ and $k_{o,y}$, the components of the output wave vector in $x$ and $y$ directions, respectively. The white plus sign marks the origin: $k_{o,x} = 0$, $k_{o,y} = 0$. The scale bar represents $k = 0.05(2\pi/\lambda)$. (c) When the input wave front tilts by $\theta_{i,y} = \tilde{\theta}_{i,y} = -7.8°$ and the output by $\theta_{o,y} = \tilde{\theta}_{o,y} = 7.1°$, the output field pattern is highly correlated to the original one in (b), with $|C_E| = 0.9$. (d) The transmitted field pattern for $\theta_{i,y} = 2.6° \neq \tilde{\theta}_{i,y}$ and $\theta_{o,y} = 2.4° \neq \tilde{\theta}_{o,y}$ is uncorrelated with that in (b), with $|C_E| = 0.05$. The conventional angular-memory-effect range is about 1°. White plus signs in (c) and (d) represent the shift of the origin ($k_{o,x} = 0 = k_{o,y}$) of the transmitted field pattern. The scale bars are identical to that in (b). Amplitude and phase patterns in (b) and (c) are shown in separate panels in Fig. S2 of the Supplemental Material [38].

The full memory (perfect correlation) in Figs. 3(a) and 3(c) is obtained from an experimentally measured transmission matrix in case of full-field (amplitude and phase) modulation of the eigenvectors. However, while injecting the eigenvectors experimentally, we use a SLM that modulates only the phase of the input field. When only the phase of an eigenvector is used, however, the correlation $|C_E(\tilde{\theta}_i, \tilde{\theta}_o)|$ drops significantly, as shown in Fig. 3(b). This is because the eigenstates of the angular memory operator consist of both high- and low-transmission eigenchannels, and the latter are strongly affected when the amplitude modulation of the input field is removed. In Fig. 3(c), all eigenstates of $Q$ have $|C_E|$ significantly less than 1 when only the phase is used. Such a dramatic reduction in $|C_E|$ due to phase-only modulation does not occur in the special case of $\tilde{\theta}_o = 0$, where the angular correlation is encoded in the input wave front (see Fig. S8 in the Supplemental Material for details [38]). To overcome the degradation at $\tilde{\theta}_o \neq 0$, we discard the low-transmission eigenchannels when computing the pseudo-inverse $(t^\dagger t)^{-1} t^\dagger$ in Eq. (2), a procedure called truncated matrix inversion. In Figs. 3(d)–3(f), among 1024 transmission eigenchannels, we keep the top 500 with high transmittance. Since the eigenstates of $Q$ comprise only these 500 eigenchannels, their robustness against the absence of amplitude modulation is notably improved. In Fig. 3(d), the correlation $|C_E|$ with full-field modulation is slightly reduced because the degree of control at the input is reduced by truncated matrix inversion, but the reduction is small. In Fig. 3(f), we plot $|C_E|$ for all eigenstates of $Q$ with phase-only modulation. The eigenstates with higher $|\alpha_n|$ have stronger correlation, because they have smaller contributions from lower transmission channels, as confirmed by their transmittance shown in Fig. S5 of the Supplemental Material [38]. In Fig. 3(e), the first eigenstate ($n = 1$) with $|\alpha_1|$ closest to 1 has $|C_E|$ above 0.73 for all input and output tilt angles $\tilde{\theta}_i$ and $\tilde{\theta}_o$, even with phase-only modulation of its incident wave front.

The robustness of the customized angular memory against the absence of amplitude modulation allows us to experimentally excite an eigenvector of the $Q(\tilde{\theta}_i, \tilde{\theta}_o)$ operator with a phase-only SLM, as shown in Fig. 4. Considering the case in Fig. 4, we display on the SLM the phase front of the first eigenstate (with the largest $|\alpha_1|$) of $Q$, which is constructed with truncated matrix inversion, keeping the top 500 transmission eigenchannels out of 1024 (see Sec. H in the Supplemental Material [38]). To tilt

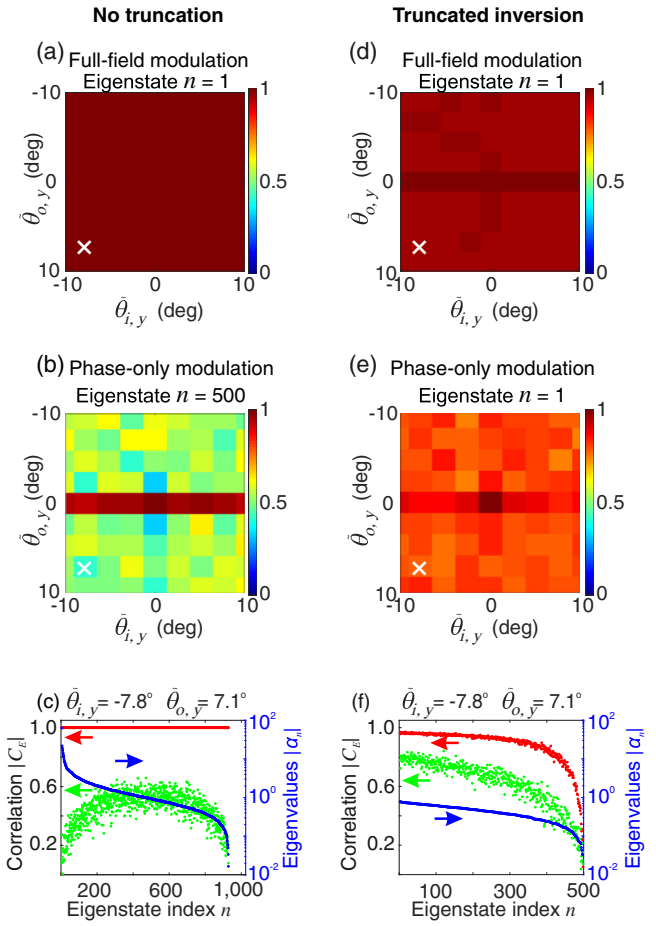


FIG. 3. Angular correlations of eigenstates and eigenvalues of $Q$. (a) All eigenstates of $Q$ customized for any combination of input and output tilt angles $\tilde{\theta}_i$ and $\tilde{\theta}_o$ have perfect correlation $|C_E| = 1$ at the chosen angles. The number of input and output channels is $N_i = N_o = 1024$. (b) Angular correlation $|C_E|$ is reduced when only the phase front of the eigenvector is modulated, except when $\tilde{\theta}_o = 0$. The eigenstate of index $n = 500$ has the highest correlation averaged over all input and output tilt angles within the range of $(-10°, 10°)$. (c) All 1024 eigenstates of $Q$ for a given pair of $\tilde{\theta}_i = -7.8°$ and $\tilde{\theta}_o = 7.1°$, marked by white × in (a) and (b), have perfect angular correlation $|C_E| = 1$ with full-field modulation of the input wave front (red, left axis). Phase-only modulation dramatically reduces the angular correlation $|C_E|$ of all eigenstates (green, left axis). (d) The truncated matrix inversion slightly reduces angular correlation for full-field modulation of the input wave front, but the first ($n = 1$) eigenstate of $Q$ with the highest $|\alpha_1|$ has $|C_E| > 0.95$ for any combination of the input and the output tilt angles $\tilde{\theta}_i$ and $\tilde{\theta}_o$. (e) With phase-only modulation of the input wave front, the truncated matrix inversion keeps $|C_E| > 0.73$ for the first eigenstate, much improved over that with no truncation in (b). (f) The truncated matrix inversion reduces the number of eigenvalues $\alpha_n$ to 500 (blue, right axis). Their angular correlation with full-field modulation (red, left axis) is compared to that with phase-only modulation (green, left axis). The angular memory eigenstate with a larger eigenvalue amplitude $|\alpha_n|$ has a higher correlation $|C_E|$. White × signs in (d) and (e) represent the selected $\tilde{\theta}_i$ and $\tilde{\theta}_o$ for $Q$. In (b), (d), and (e), the eigenstates of $Q$ have varying degree of correlation $|C_E| < 1$, and we select the one with the highest correlation averaged over all pairs of $\tilde{\theta}_i$ and $\tilde{\theta}_o$.

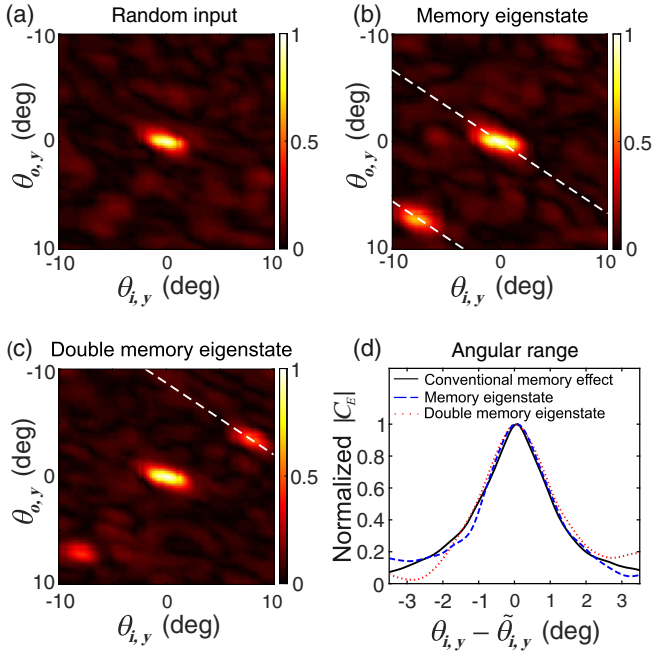


FIG. 4. Experimentally measured angular memory effect. (a) The angular correlation coefficient $|C_E|$ is enhanced only near the origin for a random input wave front. $N_i = 1024$ and $N_o = 4096$. (b) $|C_E|$ increases to 0.66 at $(\theta_{i,y} = -7.8°, \theta_{o,y} = 7.1°)$ when the incident phase front is set to that of the first eigenstate of the angular memory operator $Q$ designed for this set of angles. The conventional memory effect increases the correlation at $(\theta_{i,y} = 0, \theta_{o,y} = 0)$. (c) $|C_E|$ is enhanced at two designated angle pairs far from the origin: $|C_E| = 0.43$ at $(\theta_{i,y} = -7.8°, \theta_{o,y} = 7.1°)$ and $|C_E| = 0.5$ at $(\theta_{i,y} = 7.8°, \theta_{o,y} = -3.5°)$. White dashed lines in (b) and (c) have the slope of $n_i/n_o = 1/1.5$, where $n_i = 1.0$ is the refractive index of air on the input side of the sample and $n_o = 1.5$ is the refractive index of the glass substrate on the output side. (d) Normalized correlation functions, plotted along the white dashed lines in (b) and (c), have identical widths for conventional and customized memory effects. The customized memory effects persist over identical angular range around the chosen tilt angles compared to the conventional memory effect around $\theta_i = 0$. In (a)–(d) we experimentally display phase-only wave fronts for random input and eigenstate inputs. In (b)–(d) we construct angular memory operators using truncated matrix inversion with the 500 highest transmission eigenchannels.

the incident wave front on the sample, we laterally shift the phase front on the SLM, which is at the Fourier plane of the sample front (input) surface. The step size for input angle scanning is 0.29°, significantly smaller than the conventional angular memory effect range $\delta\theta = 1.7°$. For each tilt angle, we measure the transmitted field profile on the CCD camera with four-phase-shift interferometry. Then we tilt the transmitted wave front and compute its correlation with the original wave front. For comparison, we display a random phase front on the SLM to measure the conventional angular memory effect.

For a random input wave front, the conventional angular memory effect manifests itself as a large correlation $|C_E|$ when $\theta_{i,y}$ and $\theta_{o,y}$ are close to 0 in Fig. 4(a). Note that the memory exists only when the shift in the incident transverse wave vector equals to the shift in the outgoing transverse wave vector. When the two sides of the medium have the same refractive index, the conventional memory effect exists along the diagonal where $\theta_{i,y} = \theta_{o,y}$. In our case, the refractive index of air ($n_i = 1.0$) above the ZnO layer is lower than that of the glass substrate ($n_o = 1.5$) underneath the layer, so the conventional memory effect is tilted from the diagonal, and the white dashed line denotes $\theta_{o,y}/\theta_{i,y} = n_i/n_o = 1/1.5$. In addition, the unequal sampling rate of input and output tilt angles in our experiment contributes to the off-diagonal tilt, as detailed in Sec. I of the Supplemental Material [38].

When the SLM is configured to display the input phase front of the first eigenstate of the $Q(\tilde{\theta}_i, \tilde{\theta}_o)$ operator, $|C_E|$ is greatly enhanced at the preselected angles $\theta_{i,y} = \tilde{\theta}_{i,y} = -7.8°$ and $\theta_{o,y} = \tilde{\theta}_{o,y} = 7.1°$ of the $Q$ operator in Fig. 4(b). In spite of the phase-only modulation of input fields and a relatively large ratio $N_o/N_i = 4$, $|C_E| = 0.66$ is obtained experimentally. The phase front of the incident eigenstate, displayed on the SLM, does not exhibit any spatial correlation. As shown in Fig. S8 of the Supplemental Material, autocorrelations of both the input and the output field patterns give sharply peaked functions, confirming the angular correlation is not encoded at the input or the output fields [38]. Instead, the angular memory is created via an interplay between the spatial modulation of the incident field and the deterministic scattering of light in the disordered medium. In special cases such as $\tilde{\theta}_o = 0$ or $\tilde{\theta}_i = 0$, either the input or the output fields of the eigenstates of $Q$ feature periodic modulations; more details about these special cases are presented in Sec. K of the Supplemental Material [38].

Finally, to demonstrate the versatility of our approach, we create the angular memory simultaneously for two different input and output tilt angles. In order to realize this with a single incident wave front, we construct two angular memory operators: $Q_1(\tilde{\theta}_{i,1},\tilde{\theta}_{o,1})=(t^\dagger t)^{-1}t^\dagger X^\dagger(\tilde{\theta}_{o,1})tX(\tilde{\theta}_{i,1})$ and $Q_2(\tilde{\theta}_{i,2},\tilde{\theta}_{o,2}) = (t^\dagger t)^{-1}t^\dagger X^\dagger(\tilde{\theta}_{o,2})tX(\tilde{\theta}_{i,2})$. Then we obtain the joint operator $Q_{1+2} = (Q_1 + Q_2)/\sqrt{2}$ and find its eigenvectors with $Q_{1+2}|V_n\rangle = \alpha_n|V_n\rangle$. The phase-only modulation of the input wave front, given by the eigenvector with the highest $|\alpha_n|$, enhances the angular correlation $|C_E(\theta_i, \theta_o)|$ at two locations far from the origin in Fig. 4(c). This means the incident wave front has two memories: if tilted by 7.8° in the $-y$ direction, the transmitted wave front tilts by 7.1° in $+y$; however, if the same wave front is tilted by 7.8° in $+y$ at the input, the output wave front tilts by 3.5° in $-y$ instead. The correlation coefficients $|C_E|$ are reduced roughly by a factor of $\sqrt{2}$, compared to the case of single memory in Fig. 4(b). Such reduction is less than that of superimposing the eigenvectors of $Q_1$ and $Q_2$ in the incident wave front, which would reduce the correlation approximately by a factor 2, as shown in Sec. J of the Supplemental Material [38].

The customized memory effect holds not only at the preselected input and output angles, but also over a range around them. This behavior is similar to that of the conventional memory effect. In Fig. 4(b), with the incident wave front equal to the first eigenvector of the angular memory operator $Q(\tilde{\theta}_i, \tilde{\theta}_o)$, the correlation remains high as we scan the tilt angle $\theta_i$ of incoming wave front around $\tilde{\theta}_i$, meaning the outgoing wave front remains nearly unchanged but tilted away from $\tilde{\theta}_o$. The scanning range of the customized memory effect, given by the angular width of the normalized correlation function in Fig. 4(d), is identical to that of the conventional memory effect at the origin $(\theta_i = 0, \theta_o = 0)$. Even when we simultaneously create memories at two pairs of input and output angles in Fig. 4(c), the scanning range of the memory effect at each pair is the same as that of the conventional memory effect, as shown in Fig. 4(d).

## V. CONCLUSION

In conclusion, we have introduced a general angular memory operator $Q(\tilde{\theta}_i, \tilde{\theta}_o)$ to customize the angular memory effect for any tilt angle of the incident and the transmitted wave fronts. As long as the number of detected output channels does not exceed that of controlled input channels, the eigenstates of $Q$ exhibit perfect correlation for arbitrarily and independently chosen input and output tilt angles and directions. Experimentally, we observe strong correlations even when only the phase of the input field is modulated. Furthermore, we simultaneously create memories for different pairs of input and output tilt angles.

Although our experiment is performed on a diffusive sample with multiple scattering, our method can also be applied to a thin diffuser with forward scattering or to a multimode fiber with random mode mixing. While in the latter case the conventional angular memory effect does not even exist, our approach allows us to create any desired angular memory by launching coherent light into an eigenstate of the angular memory operator. Our approach is applicable not only to classical waves, but also to quantum waves, opening the door to customizing quantum correlations between entangled photons in complex systems [7,8]. Since memory effects exist in various domains [6,35,36,42,43], the angular memory operator can be extended to the translational memory operator, the rotational memory operator, etc. Our methodology establishes the memory effect as a versatile and flexible tool for wave front shaping applications to classical and quantum waves in complex systems.

## ACKNOWLEDGMENTS

We thank Shanti Toenger, Goëry Genty, and Arthur Goetschy for useful discussions at the initial stage of the project. This work is supported partly by the Office of Naval Research (ONR) under Grant No. N00014-20-1-2197, and by the National Science Foundation under Grant No. DMR-1905465. M. K. and S. R. acknowledge support from the European Commission under project NHQWAVE (Grant No. MSCA-RISE 691209) and from the Austrian Science Fund (FWF) under project WAVELAND (Grant No. P32300).

The authors declare no competing interests.

[1] E. Akkermans and G. Montambaux, *Mesoscopic Physics of Electrons and Photons* (Cambridge University Press, Cambridge, England, 2007).
[2] R. Berkovits and S. Feng, *Correlations in Coherent Multiple Scattering*, Phys. Rep. **238**, 135 (1994).
[3] I. Freund, *1001 Correlations in Random Wave Fields*, Waves Random Media **8**, 119 (1998).
[4] J. H. Li and A. Z. Genack, *Correlation in Laser Speckle*, Phys. Rev. E **49**, 4530 (1994).
[5] S. Schott, J. Bertolotti, J.-F. Léger, L. Bourdieu, and S. Gigan, *Characterization of the Angular Memory Effect of Scattered Light in Biological Tissues*, Opt. Express **23**, 13505 (2015).
[6] G. Osnabrugge, R. Horstmeyer, I. N. Papadopoulos, B. Judkewitz, and I. M. Vellekoop, *Generalized Optical Memory Effect*, Optica **4**, 886 (2017).
[7] H. Defienne, M. Reichert, and J. W. Fleischer, *Adaptive Quantum Optics with Spatially Entangled Photon Pairs*, Phys. Rev. Lett. **121**, 233601 (2018).
[8] O. Lib, G. Hasson, and Y. Bromberg, *Real-Time Shaping of Entangled Photons by Classical Control and Feedback*, Sci. Adv. **6**, eabb6298 (2020).
[9] I. Freund, M. Rosenbluh, and S. Feng, *Memory Effects in Propagation of Optical Waves through Disordered Media*, Phys. Rev. Lett. **61**, 2328 (1988).
[10] S. Feng, C. Kane, P. A. Lee, and A. D. Stone, *Correlations and Fluctuations of Coherent Wave Transmission through Disordered Media*, Phys. Rev. Lett. **61**, 834 (1988).
[11] R. Berkovits, M. Kaveh, and S. Feng, *Memory Effect of Waves in Disordered Systems: A Real-Space Approach*, Phys. Rev. B **40**, 737 (1989).
[12] I. Freund, M. Rosenbluh, and R. Berkovits, *Geometric Scaling of the Optical Memory Effect in Coherent-Wave Propagation through Random Media*, Phys. Rev. B **39**, 12403 (1989).
[13] A. P. Mosk, A. Lagendijk, G. Lerosey, and M. Fink, *Controlling Waves in Space and Time for Imaging and Focusing in Complex Media*, Nat. Photonics **6**, 283 (2012).
[14] I. M. Vellekoop, *Feedback-Based Wavefront Shaping*, Opt. Express **23**, 12189 (2015).
[15] S. Rotter and S. Gigan, *Light Fields in Complex Media: Mesoscopic Scattering Meets Wave Control*, Rev. Mod. Phys. **89**, 015005 (2017).
[16] S. Yoon, M. Kim, M. Jang, Y. Choi, W. Choi, S. Kang, and W. Choi, *Deep Optical Imaging within Complex Scattering Media*, Nat. Rev. Phys. **2**, 141 (2020).
[17] I. M. Vellekoop and C. Aegerter, *Scattered Light Fluorescence Microscopy: Imaging through Turbid Layers*, Opt. Lett. **35**, 1245 (2010).
[18] C. L. Hsieh, Y. Pu, R. Grange, G. Laporte, and D. Psaltis, *Imaging through Turbid Layers by Scanning the Phase Conjugated Second Harmonic Radiation from a Nanoparticle*, Opt. Express **18**, 20723 (2010).
[19] E. G. van Putten, D. Akbulut, J. Bertolotti, W. L. Vos, A. Lagendijk, and A. P. Mosk, *Scattering Lens Resolves Sub-100 nm Structures with Visible Light*, Phys. Rev. Lett. **106**, 193905 (2011).
[20] J. Bertolotti, E. G. van Putten, C. Blum, A. Lagendijk, W. L. Vos, and A. P. Mosk, *Non-Invasive Imaging through Opaque Scattering Layers*, Nature (London) **491**, 232 (2012).
[21] K. T. Takasaki and J. W. Fleischer, *Phase-Space Measurement for Depth-Resolved Memory-Effect Imaging*, Opt. Express **22**, 31426 (2014).
[22] O. Katz, P. Heidmann, M. Fink, and S. Gigan, *Non-Invasive Single-Shot Imaging through Scattering Layers and Around Corners via Speckle Correlations*, Nat. Photonics **8**, 784 (2014).
[23] H. Yılmaz, E. G. van Putten, J. Bertolotti, A. Lagendijk, W. L. Vos, and A. P. Mosk, *Speckle Correlation Resolution Enhancement of Wide-Field Fluorescence Imaging*, Optica **2**, 424 (2015).
[24] M. Cua, E. Zhou, and C. Yang, *Imaging Moving Targets through Scattering Media*, Opt. Express **25**, 3935 (2017).
[25] P. Berto, H. Rigneault, and M. Guillon, *Wavefront Sensing with a Thin Diffuser*, Opt. Lett. **42**, 5117 (2017).
[26] I. N. Papadopoulos, J.-S. Jouhanneau, J. F. A. Poulet, and B. Judkewitz, *Scattering Compensation by Focus Scanning Holographic Aberration Probing (F-SHARP)*, Nat. Photonics **11**, 116 (2017).
[27] M. Hofer, C. Soeller, S. Brasselet, and J. Bertolotti, *Wide Field Fluorescence Epi-Microscopy Behind a Scattering Medium Enabled by Speckle Correlations*, Opt. Express **26**, 9866 (2018).
[28] N. Antipa, G. Kuo, R. Heckel, B. Mildenhall, E. Bostan, R. Ng, and L. Waller, *DiffuserCam: Lensless Single-Exposure 3D Imaging*, Optica **5**, 1 (2018).
[29] O. Salhov, G. Weinberg, and O. Katz, *Depth-Resolved Speckle-Correlations Imaging through Scattering Layers via Coherence Gating*, Opt. Lett. **43**, 5528 (2018).
[30] G. Stern and O. Katz, *Noninvasive Focusing through Scattering Layers Using Speckle Correlations*, Opt. Lett. **44**, 143 (2019).
[31] A. Daniel, D. Oron, and Y. Silberberg, *Light Focusing through Scattering Media via Linear Fluorescence Variance Maximization, and Its Application for Fluorescence Imaging*, Opt. Express **27**, 21778 (2019).
[32] M. Kadobianskyi, I. N. Papadopoulos, T. Chaigne, R. Horstmeyer, and B. Judkewitz, *Scattering Correlations of Time-Gated Light*, Optica **5**, 389 (2018).
[33] M. Chen, H. Liu, Z. Liu, P. Lai, and S. Han, *Expansion of the FOV in Speckle Autocorrelation Imaging by Spatial Filtering*, Opt. Lett. **44**, 5997 (2019).

[34] M. Jang, Y. Horie, A. Shibukawa, J. Brake, Y. Liu, S. M. Kamali, A. Arbabi, H. Ruan, A. Faraon, and C. Yang, *Wavefront Shaping with Disorder-Engineered Metasurfaces*, Nat. Photonics **12**, 84 (2018).

[35] B. Judkewitz, R. Horstmeyer, I. M. Vellekoop, I. N. Papadopoulos, and C. Yang, *Translation Correlations in Anisotropically Scattering Media*, Nat. Phys. **11**, 684 (2015).

[36] T. J. Arruda, A. S. Martinez, and F. A. Pinheiro, *Controlling Optical Memory Effects in Disordered Media with Coated Metamaterials*, Phys. Rev. A **98**, 043855 (2018).

[37] H. Yılmaz, C. W. Hsu, A. Goetschy, S. Bittner, S. Rotter, A. Yamilov, and H. Cao, *Angular Memory Effect of Transmission Eigenchannels*, Phys. Rev. Lett. **123**, 203901 (2019).

[38] See Supplemental Material at http://link.aps.org/supplemental/10.1103/PhysRevX.11.031010 for detailed descriptions of the experimental setup, the measurement procedure, data analysis, and the experimental results.

[39] P. Pai, J. Bosch, M. Kühmayer, S. Rotter, and A. P. Mosk, *Scattering Invariant Modes of Light in Complex Media*, Nat. Photonics **15**, 431 (2021).

[40] S. M. Popoff, G. Lerosey, R. Carminati, M. Fink, A. C. Boccara, and S. Gigan, *Measuring the Transmission Matrix in Optics: An Approach to the Study and Control of Light Propagation in Disordered Media*, Phys. Rev. Lett. **104**, 100601 (2010).

[41] H. Yılmaz, C. W. Hsu, A. Yamilov, and H. Cao, *Transverse Localization of Transmission Eigenchannels*, Nat. Photonics **13**, 352 (2019).

[42] L. V. Amitonova, A. P. Mosk, and P. W. H. Pinkse, *Rotational Memory Effect of a Multimode Fiber*, Opt. Express **23**, 20569 (2015).

[43] N. Stasio, D. B. Conkey, C. Moser, and D. Psaltis, *Light Control in a Multicore Fiber Using the Memory Effect*, Opt. Express **23**, 30532 (2015).

# Customizing the angular memory effect for scattering media: supplementary material

Hasan Yılmaz,[1,2] Matthias Kühmayer,[3] Chia Wei Hsu,[4] Stefan Rotter,[3] and Hui Cao[1,*]

[1] *Department of Applied Physics, Yale University, New Haven, Connecticut 06520, USA*
[2] *Institute of Materials Science and Nanotechnology, National Nanotechnology Research Center (UNAM), Bilkent University, 06800 Ankara, Turkey*
[3] *Institute for Theoretical Physics, Vienna University of Technology (TU Wien), A-1040 Vienna, Austria*
[4] *Ming Hsieh Department of Electrical and Computer Engineering, University of Southern California, Los Angeles, California 90089, USA*

(Dated: April 13, 2021)

This document provides supplementary information to 'Customizing the angular memory effect for scattering media'. Here, we elaborate on the experimental setup, the measurement procedure, data analysis, and the experimental results.

## A. Scattering sample

The scattering sample is made of densely-packed zinc oxide (ZnO) nanoparticles (average diameter $\simeq$ 200 nm), deposited on a cover slip (thickness 170 µm). The ZnO layer thickness is about 10 µm. The average transmittance at $\lambda = 532$ nm is approximately 0.2.

## B. Experimental setup

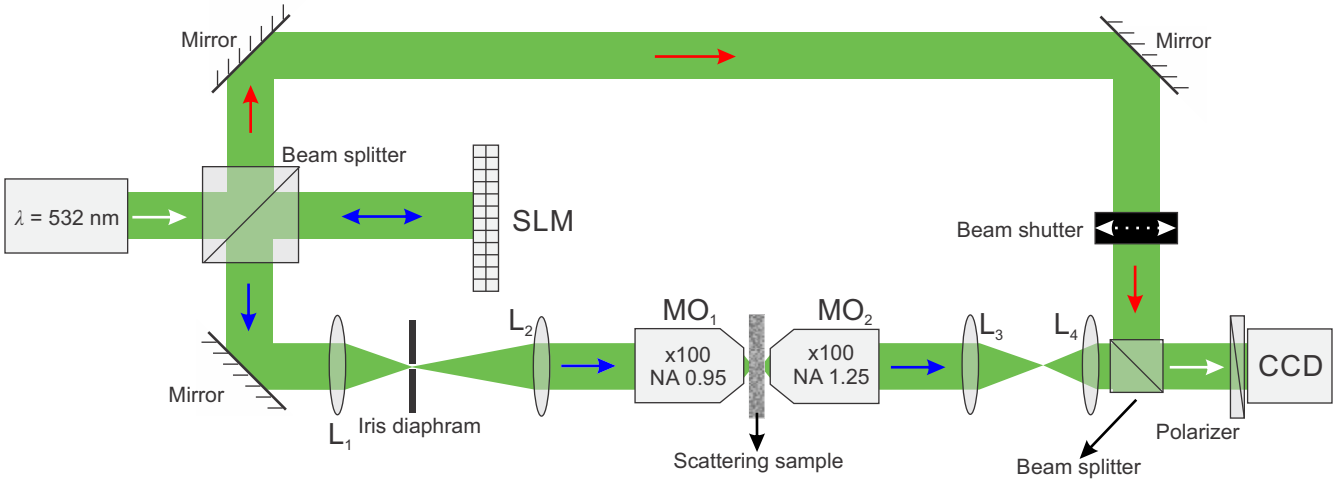


FIG. S1. **A sketch of our interferometric setup.** A reflective phase-only spatial light modulator (SLM) modulates the phase front of a monochromatic laser beam ($\lambda = 532$ nm). The field transmission matrix of the scattering sample is measured in $k$ space with the SLM and the CCD camera. $MO_{1,2}$: microscope objectives. $L_{1-4}$: lenses.

A sketch of our experimental setup is presented in Fig. S1. A linearly-polarized monochromatic laser beam (Coherent, Compass 215M-50 SL) with wavelength $\lambda = 532$ nm is expanded and collimated before splitting into two arms of the interferometer. The beam launched to the sample arm illuminates a SLM (Hamamatsu, X10468-01). The reflected beam is directed to the sample. The SLM plane is imaged onto the pupil of a microscope objective $MO_1$ (Nikon CF Plan 100×, numerical aperture $NA_{in} = 0.95$) by a pair of lenses $L_1$ and $L_2$ (with focal lengths $f_1 = 100$ mm and $f_2 = 250$ mm). An iris diaphragm between $L_1$ and $L_2$ blocks high-order diffractions from the SLM.

* hui.cao@yale.edu

The light transmitted through the sample is collected by an oil-immersion microscope objective $MO_2$ (Edmund Optics DIN Achromatic 100×, $NA_{out} = 1.25$) and collimated by a pair of lens $L_5$ ($f_5 = 200$ mm) and $L_6$ ($f_6 = 150$ mm). It then recombines with the reference beam from the other arm of the interferometer. Their interference pattern is recorded by a CCD camera (Allied Vision, Manta G-031B), which is placed at the Fourier plane of the back (output) surface of the sample. A linear polarizer in front of the camera selects one polarization component of the light.

### C. Transmission matrix measurement

The field transmission matrix from the SLM to the CCD camera is measured in Hadamard basis, with a four-phase-shift interferometry method. 2415 SLM macropixels within a circle are imaged onto the entrance pupil of $MO_1$, covering the entire pupil. Among them, we use $32 \times 32 = 1024$ macropixels inside a central square as input channels. Each macropixel consists of $9 \times 9$ SLM pixels. A high-spatial-frequency phase grating is written outside the central square on the SLM to diffract the light away from the iris diaphram.

By applying four global phases in between 0 and $2\pi$ to the Hadamard phase patterns on the $32 \times 32$ SLM macropixels, we retrieve the phase difference between the transmitted field pattern and the reference beam with a flat phase front from their interference patterns on the CCD camera. Finally, we block the reference beam with a beam shutter, and measure the transmitted intensity patterns of the 1024 Hadamard phase pattern inputs. Combining the measured phase pattern and the amplitude pattern of the transmitted light, we obtain the complex field pattern.

In this setup, we modulate a single linear polarization of light at the input, and detect a single linear polarization of light at the output. Experimentally we measure the transmitted field pattern within a square on the CCD camera that has $64 \times 64 = 4096$ pixels. The transmission matrix $t$ is a $N_o \times N_i$ matrix, where $N_i = 1024$ is the number of SLM macropixels, $N_o = 4096$ is the number of CCD camera pixels.

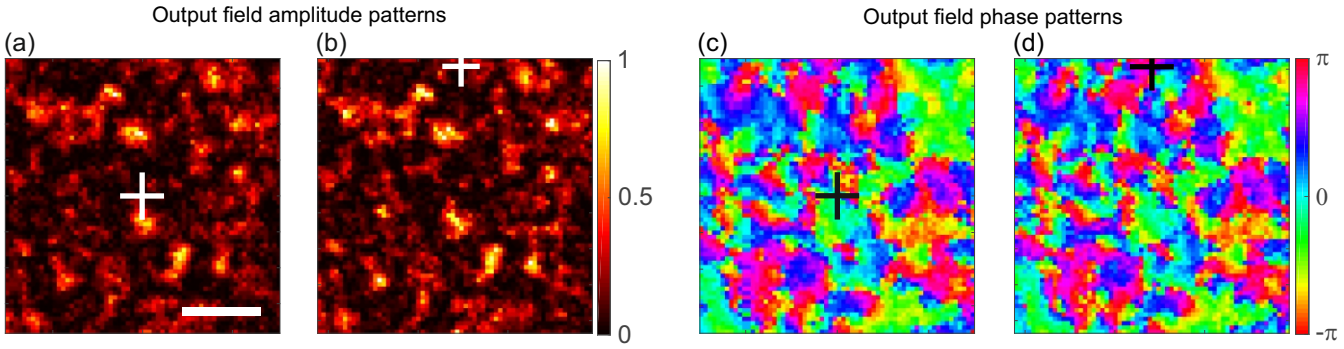


FIG. S2. **Output patterns of an angular memory eigenstate.** Amplitude **(a,b)** and phase **(c,d)** patterns of the transmitted complex fields in Fig. 2(b,c) of the main text are shown separately. The Pearson correlation coefficient between the amplitude patterns is 0.82 and between the phase patterns is 0.83. The horizontal and vertical axes represent $k_{o,x}$ and $k_{o,y}$, the components of the output wavevector in $x$ and $y$ directions, respectively. The white/black plus signs mark the origin: $k_{o,x} = 0$, $k_{o,y} = 0$. The scale bar represents $k = 0.05(2\pi/\lambda)$.

### D. Rotation operator and edge effects

Here we elaborate on the rotation operators $X$ that tilt the incoming and outgoing field profiles, in Eqs. (1) and (2) of the main text. $X$ can be expressed as a matrix. For the illustration purpose, let us first consider a 2D scattering medium whose 1D cross-section is parallel to $y$ axis and light transmitting along $z$ axis. The transmission matrix $t$ is given in the momentum space, mapping the input transverse wavevectors $k_y$ to the output ones. Tilting the incident wavefront by an angle $\theta_i$ corresponds to shifting input $k_y$ to $k_y + \Delta k_y$, where $\Delta k_y = k \sin\theta_i$ and $k = 2\pi/\lambda$. Since each column of the transmission matrix represents an input $k_y$, a shift of input $k_y$ is equivalent to a lateral shift of matrix columns, which is done by multiplying the $t$ matrix by a matrix $X$ whose elements are equal to zero except on a line parallel to the matrix diagonal. Its distance to the diagonal is determined by the amount of shift $\Delta = k \sin\theta_i / \delta k_y$, where $\delta k_y$ is the sampling step of input $k_y$ for the $t$ matrix. The matrix $X$ element $X_{p\,q} = \delta_{p\,q+\Delta}$, i.e., only for $p = q + \Delta$, the value is equal to 1, otherwise it is equal to 0. Similar argument holds for tilting the transmitted wavefront by shifting the $t$ matrix rows. Next we consider a 3D scattering medium whose 2D cross-section is parallel to $x - y$ plane. Although the expression of matrix $X$ is more complicated, its function is to move the transmission

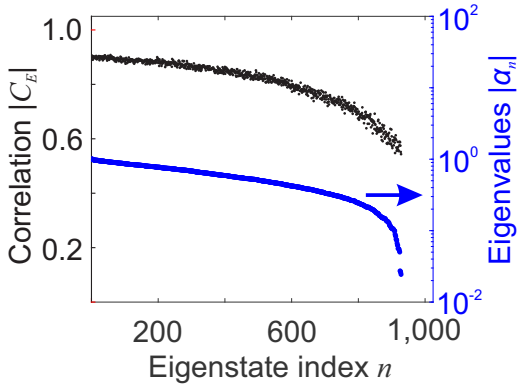


FIG. S3. **Correlations and eigenvalues of the angular memory eigenstates.** The angular memory operator $Q$, which is identical to that in Fig. 2 of the main text, has 1024 eigenstates, are ordered by their eigenvalue amplitude $|\alpha_n|$ (blue). Their angular correlation coefficient $|C_E|$ (black) drops with $|\alpha_n|$. The first eigenstate ($n = 1$) with the highest $|\alpha_n|$ exhibit the strongest angular correlation.

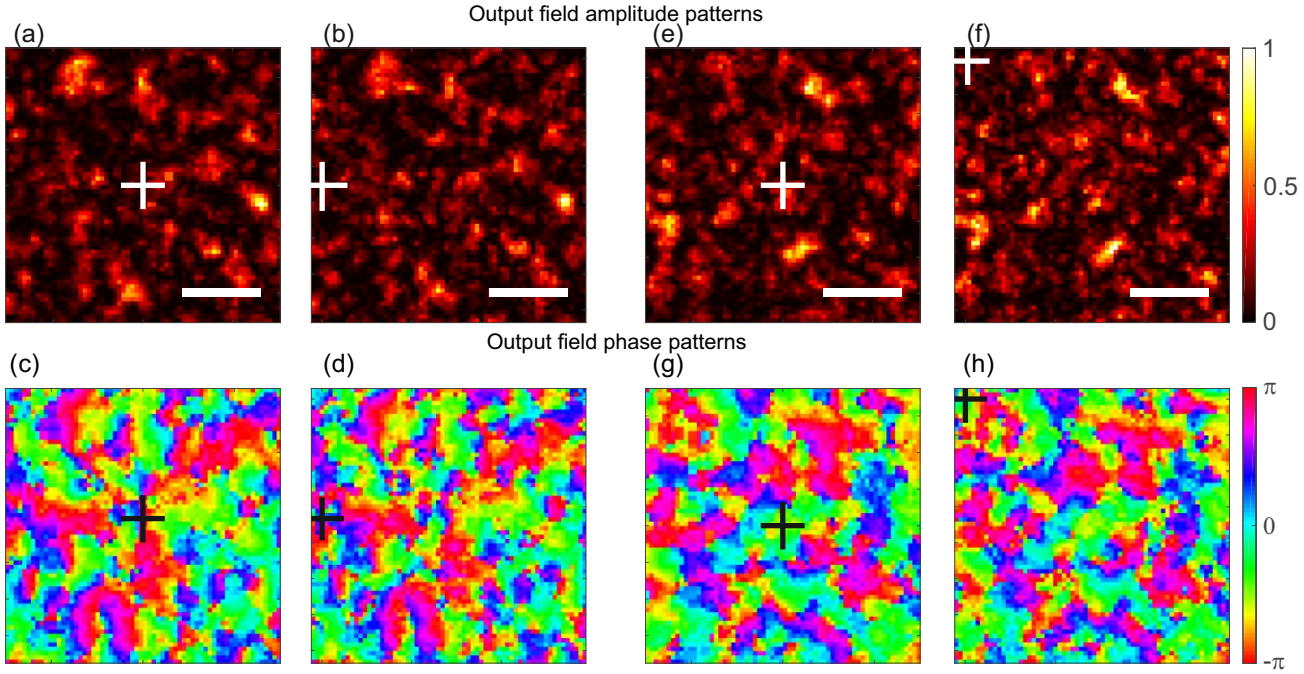


FIG. S4. **Two angular memory eigenstates with different tilt directions of the input and the output wavefronts. (a-d)** Amplitude (a,b) and phase (c,d) patterns of the transmitted fields for an angular memory eigenstate with the input field tilted in $-y$ by 7.8° and the output field tilted in $x$ by 7.1° are shown. **(e-h)** Amplitude (e,f) and phase (g,h) patterns of the transmitted fields for an angular memory eigenstate with the input field tilted in $-y$ by 7.8° and the output field tilted in the diagonal direction $\hat{x} + \hat{y}$ by 7.1° are shown. The white/black plus signs mark the origin, and the scale bars are identical to those in Fig. S2.

matrix elements $t_{m\,n}$ to $t_{m\,n+\Delta}$ for tilting the input wavefront, or to $t_{m+\Delta\,n}$ for tilting the output wavefront, where $\Delta$ is proportional to the tilt angle.

To avoid any edge effect in tilting, we experimentally measure the transmission matrix over a large angular range, e.g., from −20° to 20° for both input and output angles, and then crop the matrix to −10° to 10°. While shifting the matrix columns or rows, we resort to the original large matrix and shift the columns or rows first before cropping. This will allow us to tilt from −10° to 10° without any edge effect.

### E. Angular memory operator

In the main text, we show that the additional term $(t^\dagger t)^{-1}$ counter-balances the increase of the denominator of the angular correlation coefficient. Alternatively, one can use $\{[X^\dagger(\tilde{\theta}_o)tX(\tilde{\theta}_i)]^\dagger X^\dagger(\tilde{\theta}_o)tX(\tilde{\theta}_i)\}^{-1}$, and obtain the same operator given in Eq. 2 of the main text. First, we start with the definition $Q'$ below by multiplying $Q_0$ with $\{[X^\dagger(\tilde{\theta}_o)tX(\tilde{\theta}_i)]^\dagger X^\dagger(\tilde{\theta}_o)tX(\tilde{\theta}_i)\}^{-1}$ from the right as

$$Q' \equiv t^\dagger X^\dagger(\tilde{\theta}_o)tX(\tilde{\theta}_i)\{[X^\dagger(\tilde{\theta}_o)tX(\tilde{\theta}_i)]^\dagger X^\dagger(\tilde{\theta}_o)tX(\tilde{\theta}_i)\}^{-1}. \tag{S1}$$

When $t$ is an $N_o \times N_i$ square matrix ($N_o = N_i$), $[t^\dagger]^{-1}$ exists, therefore the relation above can be simplified to

$$Q' = t^\dagger X^\dagger(\tilde{\theta}_o)[t^\dagger]^{-1}X(\tilde{\theta}_i). \tag{S2}$$

Using the left eigenvalue decomposition as $\langle V_n|\, t^\dagger X^\dagger(\tilde{\theta}_o)[t^\dagger]^{-1}X(\tilde{\theta}_i) = \langle V_n|\, \alpha'_n$ we obtain $\langle V_n|\, t^\dagger = \langle V_n|\, [X^\dagger(\tilde{\theta}_i)t^\dagger X(\tilde{\theta}_o)]\alpha'_n$, which is identical to

$$t\,|V_n\rangle = \alpha'^\dagger_n[X^\dagger(\tilde{\theta}_o)tX(\tilde{\theta}_i)]\,|V_n\rangle\,. \tag{S3}$$

### F. Angular memory eigenstates

Fig. 2 in the main text shows that when the incident wavefront of an angular memory eigenstate is tilted by 7.8° in $-y$ direction, the transmitted field pattern tilts by 7.1° in $+y$ direction. In Fig. 2(b,c), the complex fields in transmission are plotted in such a way that the brightness is proportional to the field amplitude and the color represents phase. In Fig. S2(a-d), we plot the amplitude and phase patterns of the transmitted fields to show their similarities separately.

Here, the measured transmission matrix $t$ is a rectangular matrix with $N_o = 4096 > N_i = 1024$. When $t$ is a rectangular matrix with $N_o > N_i$, we construct the angular memory operator $Q(\tilde{\theta}_i, \tilde{\theta}_o) = (t^\dagger t)^{-1}t^\dagger X^\dagger(\tilde{\theta}_o)tX(\tilde{\theta}_i)$ using the left inverse of $t_{4096\times1024}$ as $(t^\dagger t)^{-1}t^\dagger$. $Q$ has 1024 eigenvalues $\alpha_n$ ($n = 1, 2, ..., 1024$), and the corresponding eigenstates are ordered by $|\alpha_n|$ from high to low, as shown in Fig. S3. The angular correlation $|C_E|$ increases with $|\alpha_n|$, and the first eigenstate ($n = 1$) with the largest $|\alpha_1|$ has the strongest correlation, as shown in Fig. 2 of the main text.

### G. Customized angular memory effect

In Fig. S2, input and output wavefronts are tilted in opposite directions along the $y$ axis. In Fig. S4(a-h), we construct different eigenstates of $Q$ to customize the angular memory effect, such that when the input wavefront is tilted in $y$ direction, the output wavefront tilts in $x$ direction or diagonal direction $\hat{x} + \hat{y}$.

### H. Phase-only modulation with truncated matrix inversion

The left inverse $(t^\dagger t)^{-1}t^\dagger$ reduces to $t^{-1}$, when $t$ is a square matrix with $N_o = N_i$ such as in Fig. 3 of the main text. Perfect angular correlation $|C_E| = 1$ is achieved with full-field (amplitude and phase) modulation of the input wavefront in Fig. 3(a). However, phase-only modulation of the input field reduces $|C_E|$ significantly, as seen in Fig. 3(b). This is caused by the low-transmission eigenchannels constituting an eigenvector of angular memory operator $Q$.

In order to couple light into angular memory eigenstates with phase-only modulation of the incident wavefront in experiments, we must discard the low-transmission eigenchannels that are sensitive to the absence of amplitude modulation. To remove the low-transmission eigenchannels, we first conduct the singular value decomposition $t = U_n\Sigma_n V_n^\dagger$, where the columns of $V_n$ and $U_n$ represent the input and the output wavefronts of the transmission eigenchannels, respectively, and the diagonal elements of $\Sigma_n$ gives the singular values, which are the square root of the transmission eigenvalues. Then we use the left inverse of $t$, which is given by $(t^\dagger t)^{-1}t^\dagger = V_n(\Sigma_n^\dagger\Sigma_n)^{-1}\Sigma_n^\dagger U_n^\dagger$. Next we truncate the singular values by keeping only the first 500 diagonal elements in $(\Sigma_n^\dagger\Sigma_n)^{-1}\Sigma_n^\dagger$ (corresponding to keeping the reciprocal of 500 highest singular values), and replacing the remaining 524 diagonal elements of $(\Sigma_n^\dagger\Sigma_n)^{-1}\Sigma_n^\dagger$ by zero. Finally we build the angular memory operator $Q(\tilde{\theta}_i, \tilde{\theta}_o) = (t^\dagger t)^{-1}t^\dagger X^\dagger(\tilde{\theta}_o)tX(\tilde{\theta}_i)$ and find its eigenvectors. The

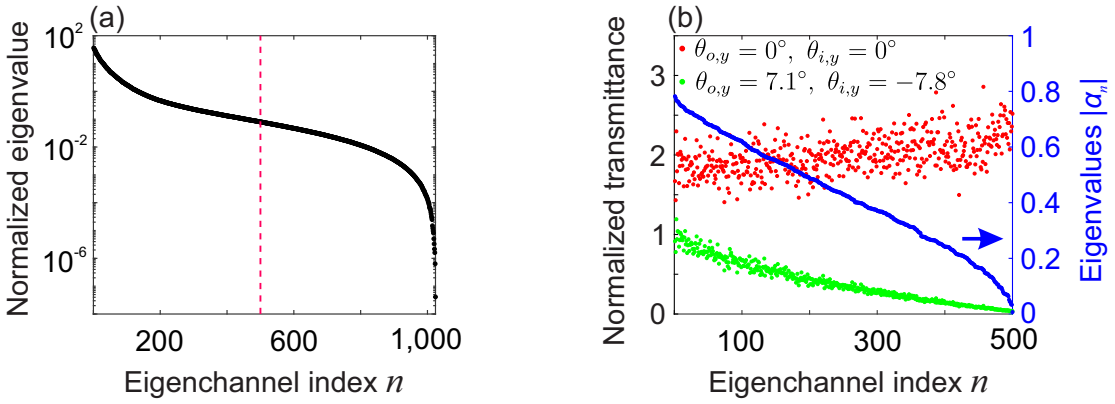


FIG. S5. **Transmission matrix truncation. (a)** The square of the singular values of the $N_o \times N_i = 1,024 \times 1,024$ transmission matrix $t$ in Fig. 3 of the main text represent the transmittance (transmission eigenvalues) of 1024 transmission eigenchannels. The red vertical line denotes the threshold we choose to discard 524 transmission eigenchannels with a transmittance below it. Phase-only-modulated angular memory eigenstates that comprise only of 500 transmission eigenchannels with transmittance above the threshold have improved angular correlation $|C_E|$, as shown in Fig. 3(e,f) of the main text. **(b)** Transmittance of all angular memory eigenstates $T_n$ with the original (red) or tilted wavefronts (green) are normalized by that of transmittance of a random input wavefront. A larger eigenvalue amplitude $|\alpha_n|$ (blue) corresponds to a higher transmittance for the tilted wavefronts, while the transmittance for the original (untilted) wavefront is nearly constant.

truncated matrix inversion results in using the 500 highest-transmission eigenchannels to construct the eigenvectors of $Q$, making them robust to phase-only modulation in our experiment.

Fig. S5(a) shows all transmission eigenvalues, corresponding to the transmittance of 1024 transmission eigenchannels. The red vertical line marks the threshold we choose for the truncated matrix inversion in Fig. 3(d-f) of the main text. 524 transmission eigenchannels with a transmittance below this threshold are discarded. The remaining 500 transmission eigenchannels constitute the eigenvectors of $Q$ operator. The angular correlation $|C_E|$ is significantly improved, as shown in Fig. 3(e) of the main text. The eigenstates with higher $|\alpha_n|$ have stronger correlation, because they have less contributions from lower transmission eigenchannels. This is confirmed by their transmittance shown in Fig. S5(b). The truncated matrix inversion is also used to obtain the results in Figs. 4 and S8 where we experimentally display the phase fronts of the eigenvectors on the SLM.

## I. Angular correlation measurement

After finding the eigenstates of $Q$, we display the phase pattern of the first eigenstate with the highest eigenvalue amplitude on the 1024 macropixels of the SLM, and measure the phase pattern of the light field transmitted through the sample with four-phase-shift interferometry method. We gradually shift the phase pattern of the eigenvector on the SLM to tilt its wavefront incident on the sample, and measure the transmitted phase patterns for each tilt angle of input $\theta_i$. Although the transmission matrix is measured with SLM macropixels (each containing $9 \times 9$ pixels), we laterally shift the input phasefront with the step size of *single* pixel on the SLM. Thus the input tilt angle is scanned at the step size of $0.29°$. The scanning range is $(-10°, 10°)$, significantly larger than the angular correlation range $\delta\theta = 1.7°$ of the random wavefronts. Then we block the reference beam using a beam shutter, and measure the transmitted intensity pattern to recover the complex field profile. We repeat this measurement with a random incident wavefront to obtain the correlation function for conventional angular memory effect.

In the main text, we state two causes of the off-diagonal tilt of the measured angular correlation in Fig. 4: (i) refractive index mismatch on the input and output sides of the sample, and (ii) unequal sampling rate of input and output angles. Below we illustrate (ii) in a numerical simulation. Experimentally the sampling step of input tilt angle $\theta_i$ is larger than that of output tilt angle $\theta_o$ (given by the CCD camera pixel size). The measured angular correlation function $C_E$ can be simulated by convolution with the input and output angular point spread function (PSF). If the sampling step of $\theta_i$ is equal to that of $\theta_o$, the 2D PSF is isotropic and represented by a circle in Fig. S6(a). The convolved correlation is along the white line whose slope is equal to the ratio $n_i/n_o$ of refractive indices at input and output sides of the sample. However, when the input sampling step is larger than the output one, the 2D PSF is elongated horizontally, and the convolved correlation is tilted slightly towards the horizontal axis. This result agrees with the experimental data in Fig. 4 in the main text, confirming the effect of sampling rate on the angular correlation

function.

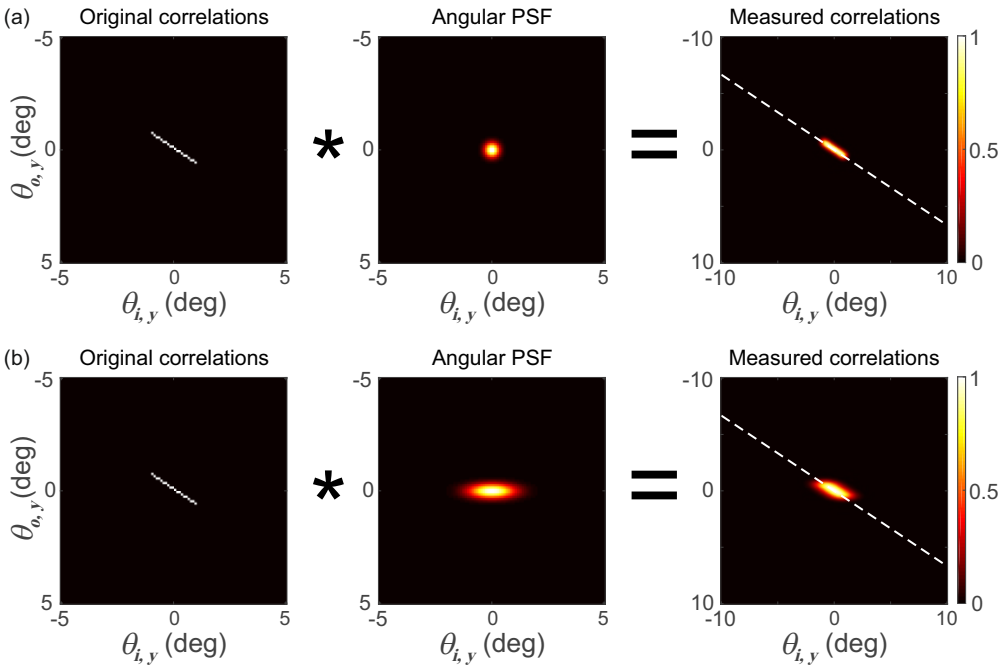


FIG. S6. **Effect of sampling rate on the angular correlation function.** The first column shows the angular correlation function tilted away from the diagonal due to refractive index mismatch at input and output sides of the sample. The second column shows the angular PSF, which is determined by the sampling steps of input and output angles. The last column is simulation of measured correlation function which is a convolution of the first and second columns. **(a)** The sampling steps of input and output angles are identical, the angular PSF is isotropic, and the tilt of the angular correlation function from the diagonal is determined by the refractive index mismatch (dashed white line). **(b)** The sampling step of input angle is larger than that of output angle, the PSF is elongated horizontally, and the correlation function is tilted further towards the horizontal axis.

### J. Creating double memories

In the main text, we create the angular memory simultaneously at two pairs of input and output tilt angles, by setting the incident wavefront to an eigenstate of a joint operator $Q_{1+2} = [Q_1(\tilde{\theta}_{i,1}, \tilde{\theta}_{o,1}) + Q_2(\tilde{\theta}_{i,2}, \tilde{\theta}_{o,2})]/\sqrt{2}$. Alternatively, double memories can be obtained by superposing the eigenstates of the two operators $(V_n^{(1)} + V_n^{(2)})/\sqrt{2}$, where $Q_1 V_n^{(1)} = \alpha_n^{(1)} V_n^{(1)}$ and $Q_2 V_n^{(2)} = \alpha_n^{(2)} V_n^{(2)}$.

We compute the angular correlations in these two cases, and compare to that of single memory. Fig. S7(a) shows the correlation coefficient $|C_E(\theta_{i,y}, \theta_{o,y})|$ for the first eigenvector $V_1^{(1)}$ of $Q_1(\tilde{\theta}_{i,y} = 7.8°, \tilde{\theta}_{o,y} = -3.5°)$ with the largest eigenvalue amplitude $|\alpha_1^{(1)}|$. The maximum correlation at $\theta_{i,y} = \tilde{\theta}_{i,y} = 7.8°, \theta_{o,y} = \tilde{\theta}_{o,y} = -3.5°)$ is $|C_E| = 0.88$. In Fig. S7(b), we compute the angular correlation for the incident wavefront $(V_1^{(1)} + V_1^{(2)})/\sqrt{2}$, where $V_1^{(2)}$ is the first eigenvector of $Q_2(\tilde{\theta}_{i,y} = -7.8°, \tilde{\theta}_{o,y} = 7.1°)$ with the largest eigenvalue amplitude $|\alpha_1^{(2)}|$. The maximum correlations at the preselected angles, $|C_E(7.8°, -3.5°)| = |C_E(-7.8°, 7.1°)| = 0.46$, are reduced approximately by a factor of 2 from that of single memory in Fig. S7(a). Fig. S7(c) shows the angular correlation for the incident wavefront being the first eigenvector of the joint operator $Q_{1+2}$ which has the largest eigenvalue amplitude $|\alpha_1^{(1+2)}|$. The correlations at the two pairs of designated angles are $|C_E(7.8°, -3.5°)| = 0.68$ and $|C_E(-7.8°, 7.1°)| = 0.63$. Hence, the decrease from the single memory is about $\sqrt{2}$. These results confirm that it is more efficient to create double memories with the eigenvectors of the joint angular memory operator than superposing the eigenvectors of separate operators.

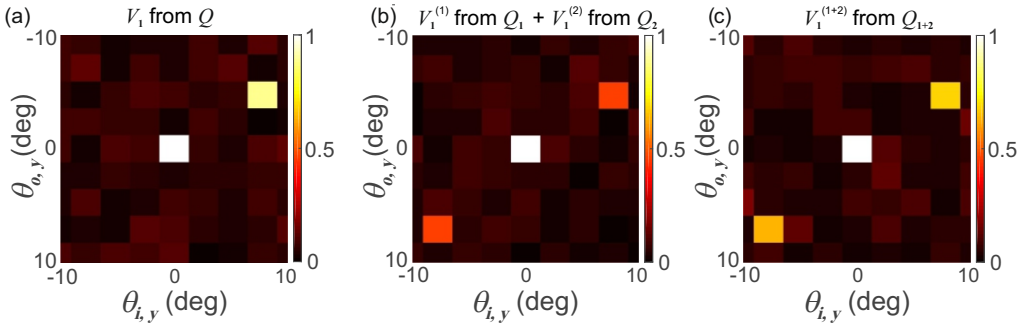


FIG. S7. **Single memory versus double memories. (a)** Angular correlation $|C_E(\theta_{i,y}, \theta_{o,y})|$ for the incident wavefront equal to the first eigenvector $V_1^{(1)}$ of the angular memory operator $Q_1(\tilde{\theta}_{i,y} = 7.8°, \tilde{\theta}_{o,y} = -3.5°)$. The number of controlled input channels is $N_i$ = 1,024, and the number of detected output channels is $N_o$ = 4,096. **(b)** Superposing the first eigenvectors of two operators $Q_1(\tilde{\theta}_{i,y} = 7.8°, \tilde{\theta}_{o,y} = -3.5°)$ and $Q_2(\tilde{\theta}_{i,y} = -7.8°, \tilde{\theta}_{o,y} = 7.1°)$ in the incident wavefront reduces the maximum correlation by a factor of 2 to $|C_E| = 0.46$. **(c)** The first eigenvector of a joint operator $Q_{1+2} = (Q_1 + Q_2)/\sqrt{2}$ enhances the correlations at two pairs of input and output angles: $|C_E(7.8°, -3.5°)| = 0.68$ and $|C_E(-7.8°, 7.1°)| = 0.63$. These values are roughly a factor of $\sqrt{2}$ lower than that of single memory in (a).

### K. Two special cases

Finally, we investigate the eigenstates of the angular memory operator in two special cases: (i) output tilt angle $\tilde{\theta}_o = 0$; (ii) input tilt angle $\tilde{\theta}_o = 0$.

For comparison, we show the experimentally measured $|C_E(\theta_i, \theta_o)|$ for a random phase front of the input field in Figs. S8(a-c). In (a), $|C_E|$ exhibits conventional memory effect correlation around the origin ($\theta_i = 0, \theta_o = 0$). The autocorrelation functions of input field pattern in (b) and of output in (c) vanish away from the origin, indicating there is no spatial correlation in the input or the output wavefront.

Fig. S8(d), which is the same as Fig. 4(a) of the main text, shows the measured $|C_E(\theta_i, \theta_o)|$ for the first eigenstate of angular correlation operator $Q(\tilde{\theta}_{i,y} = -7.8°, \tilde{\theta}_{o,y} = 7.1°)$. The autocorrelation functions of the input and output field profiles in (e) and (f) are identical to those of a random input. Hence, there is no correlation in both the input and the output field patterns for this eigenstate with $\tilde{\theta}_i \neq 0$ and $\tilde{\theta}_o \neq 0$.

Fig. S8(g-i) represent the first special case: $\tilde{\theta}_{i,y} = -7.8°$, $\tilde{\theta}_{o,y} = 0$. In Fig. S8(g), the experimentally measured $|C_E|$ is enhanced not only at $(\theta_{i,y} = -7.8°, \theta_{o,y} = 0)$ as intended, but also at $(\theta_{i,y} = 7.8°, \theta_{o,y} = 0)$. This phenomenon originates from the periodic modulation of the input field, as confirmed by the autocorrelation function of the input field pattern in (h), which reveals the modulation period is equal to 7.8°. The output field pattern has no spatial correlation, as seen from its autocorrelation function in (i).

Fig. S8(j-l) illustrate the second special case: $\tilde{\theta}_{i,y} = 0$, $\tilde{\theta}_{o,y} = -7.1°$. $|C_E|$ is enhanced not only at $(\theta_{i,y} = 0, \theta_{i,y} = -7.1°)$ as intended, but also at $(\theta_{i,y} = 0, \theta_{i,y} = 7.1°)$ in Fig. S8(j). According to its autocorrelation function in Fig. S8(l), the output field pattern is periodically modulated with a period of 7.1°. The input field pattern has no correlation, as confirmed by its autocorrelation function in Fig. S8(k).

These two special cases are examples of encoding angular memories into the input or output wavefronts.

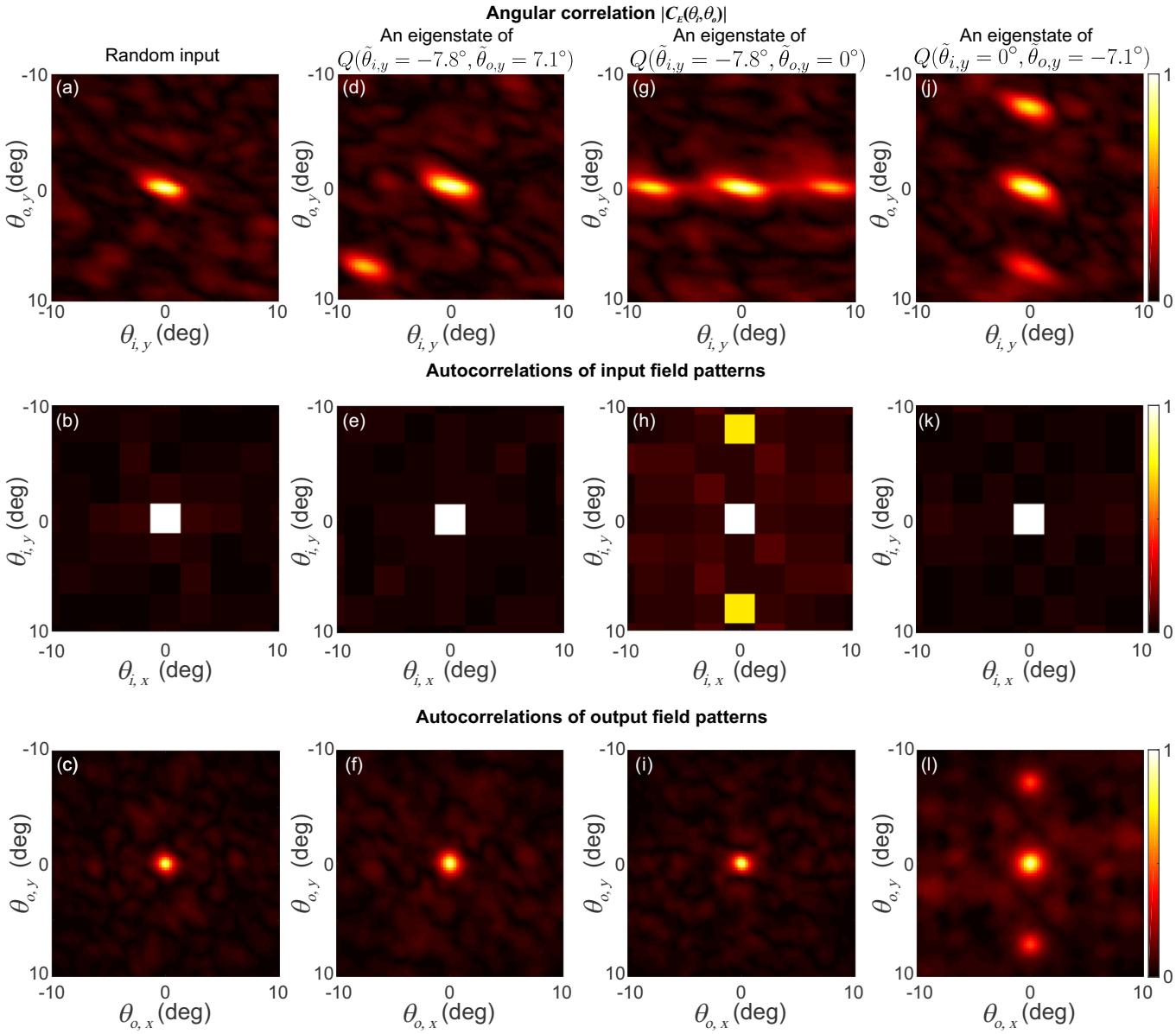


FIG. S8. **The angular memories and the autocorrelations of the input and the output fields.** First row: correlation coefficient $|C_E(\theta_{i,y},\theta_{o,y})|$ is shown, where $\theta_{i,y}$ represents the input tilt angle, and $\theta_{o,y}$ the output tilt angle in $y$ direction. The input wavefront is random in **(a)**, equal to an angular memory eigenstate of $Q(\tilde{\theta}_{i,y}=-7.8^\circ,\tilde{\theta}_{o,y}=7.1^\circ)$ in **(d)**, $Q(\tilde{\theta}_{i,y}=-7.8^\circ,\tilde{\theta}_{o,y}=0)$ in **(g)**, $Q(\tilde{\theta}_{i,y}=0,\tilde{\theta}_{o,y}=-7.1^\circ)$ in **(j)**. Second row: autocorrelations of input field patterns for (a,d,g,j) are shown in **(b,e,h,k)**, revealing periodic modulation of input field in (h). Third row: autocorrelations of output field patterns for (a,d,g,j) are shown in **(c,f,i,l)**, revealing periodic modulation of output fields in (l). The rest input and output field patterns have no spatial correlations. $N_i = 1024$, $N_o = 4096$. Here, we use the truncated matrix inversion by keeping the first 500 singular vectors with the highest 500 singular values. In all cases, we experimentally display the phase front of the eigenvector with the highest eigenvalue $|\alpha_n|$ and measure the output field patterns with the four-phase-shift interferometry method.